Computational modeling of classical and ablative Rayleigh–Taylor instabilities

W.M. WOOD-VASEY[1,*] K.S. BUDIL,[2] B.A. REMINGTON,[2] S.G. GLENDINNING,[2]
A.M. RUBENCHIK,[2] M. BERNING,[2] J.O. KANE,[2] AND J.T. LARSEN[2]

[1]Harvey Mudd College, Claremont, CA 91711
[2]Lawrence Livermore National Laboratory, Livermore, CA 94550

Abstract

Modeling plus simulations using the one-dimensional Lagrangian radiation-hydrodynamics code HYADES are compared with data from classical and ablative Rayleigh–Taylor experiments conducted on the Nova laser. Comparisons between the experiments and modeling for both the gross hydrodynamic motion and the perturbation evolution are made and show good agreement. A third order perturbation analysis is applied to demonstrate the onset of nonlinearity. A simple, physically intuitive saturation model is used to describe the growth further into the nonlinear regime. Finally, we present the first comparison of the Betti ablation front theory with indirect-drive RT data and obtain good agreement.

Keywords: Linear; Modeling; Nonlinear; Rayleigh–Taylor instability

1. INTRODUCTION

Hydrodynamic instabilities arise in a variety of fields, ranging from large-scale astrophysical phenomena such as supernovae (Muller *et al.*, 1991; Herant & Woosley, 1994) to the implosion of inertial confinement fusion (ICF) capsules (Lindl & Mead, 1975; Takabe *et al.*, 1983). Each of these systems, which can consist of many layers of fluids of different densities, undergoes a temporal evolution characterized by periods of radial acceleration or deceleration and the passage of one or more shocks. These conditions give rise to several commonly discussed hydrodynamic instabilities such as the Rayleigh–Taylor (Chandrasehkar, 1968) and Richtmyer–Meshkov (Richtmyer, 1960; Meshkov, 1969) instabilities. In this work we focus on the Rayleigh–Taylor (RT) instability in laser-driven experiments.

The RT instability occurs when a heavier fluid is accelerated by a lighter fluid and is important at both ablative and embedded interfaces. The growth of ablation front perturbations has been shown to be reduced relative to the growth of perturbations at an embedded, or classical, interface due to the stabilizing effects of ablation and density gradients. (Budil *et al.*, 1996) While the RT instability is seen as a

smooth, constant acceleration in the ideal case, the RM instability is the opposite extreme of an impulsive acceleration of an interface between two fluids of different densities.

Since complex physical systems such as ICF capsules tend to undergo a series of shock transversals and accelerations, an understanding of both of these instabilities and their interaction is crucial. To test our abilities to model and understand such systems, planar hydrodynamic instability experiments were conducted on the Nova laser, as illustrated schematically in Figure 1 (Budil *et al.*, 1996; Remington *et al.*, 1992, 1995). Data analysis and preliminary modeling showed nearly classical RT growth at the embedded interface, with the largest growth factors occurring at the shortest wavelengths, as shown by the dashed curve in Figure 2. Conversely, at the ablation front, RT growth of the shortest wavelength perturbations was significantly inhibited, as illustrated by the solid curve. In this paper we describe the details behind the two calculations shown in Figure 2.

2. RADIATION HYDRODYNAMICS SIMULATION

2.1. Experiment

The design used in these experiments is shown in Figure 1 and is described in more detail elsewhere (Budil *et al.*, 1996; Remington *et al.*, 1992, 1995). We studied planar foils with
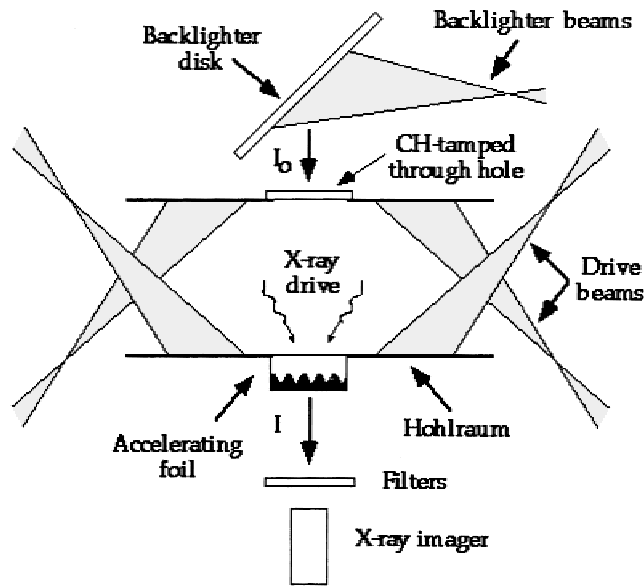
Fig. 1. A schematic representation of the experiment. Eight beams of the Nova laser are used to create an x-ray drive inside of the hohlraum which accelerates the CH(Br) pusher (white) into the Ti payload (black). The remaining two beams are used to irradiate backlighter foils (Fe or Mo) to generate X rays for side-on or face-on radiography.

Fig. 3. Characteristic laser power (solid curve) and radiation drive temperatures T_r (dashed curve) profiles for these experiments. The simulations used standard T_r profiles that were scaled by the laser powers of each shot: $T_{r_1} = (P_2/P_1)^{1/4} T_r$.

embedded or ablation front interfaces accelerated by the X-ray drive generated by high-intensity laser beams incident on a gold hohlraum inside of the Nova laser chamber. The embedded interface (classical RT or CRT) targets were composed of a 35 μm thick foil, or "ablator," of brominated plastic ($C_{50}H_{47}Br_3$, hereafter referred to as CH(Br)) of den-

sity $\rho = 1.26$ g/cm^3 backed by a 15 μm thick titanium (Ti) payload of density $\rho = 4.5$ g/cm^3 with a well-characterized initial perturbation machined at the CH(Br)-Ti interface. The ablation front RT targets consisted of 50–60 μm of CH(Br) with the initial perturbation molded into the ablation front side of the target. The 750 μm diameter experimental packages were mounted onto a 3 mm long × 1.6 mm diameter gold cylindrical hohlraum which was driven by 8 beams of the Nova laser at 3ω (where ω refers to the base frequency of the original input laser), $\lambda = 350$ nm, in a 3.3 ns shaped pulse. Nova is capable of generating laser light at $\lambda = 1056$, 528, and 350 nm, which corresponds to frequencies of ω, 2ω, and 3ω, respectively.

Figure 3 shows the total representative laser power profile used in the experiments and the corresponding radiation temperature generated in the hohlraum. Figure 4 shows the drive spectrum corresponding to the radiation drive near peak power. The solid line in Figure 4 is a measured spectrum from a Nova experiment while the dashed line represents a Planckian blackbody spectrum at 173 eV. As can be seen in the figure, the spectral energy density does not decrease as rapidly as a Planckian distribution at photon energies $\geqq 2$ keV. The L-edge of Br is at 1.7 keV (dark vertical line), and the Br doped into the CH serves as a partial shield against X-ray preheat.

The remaining two Nova beams at 2ω, $\lambda = 528$ nm, were focused in a 3 ns square pulse onto either an iron (for the embedded interface targets) or molybdenum (for the ablation front targets) disk to generate a hard X-ray source to back-illuminate the accelerating foils. The Fe foil generated a backlighter spectrum dominated by He-α X-rays at 6.7 keV while the Mo spectrum was dominated by a broad L-band centered around 2.6 keV. To obtain optical density measurements to be later converted into relative perturbation ampli-
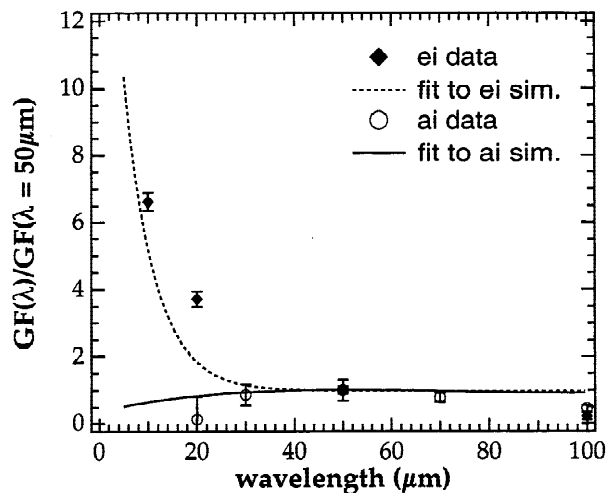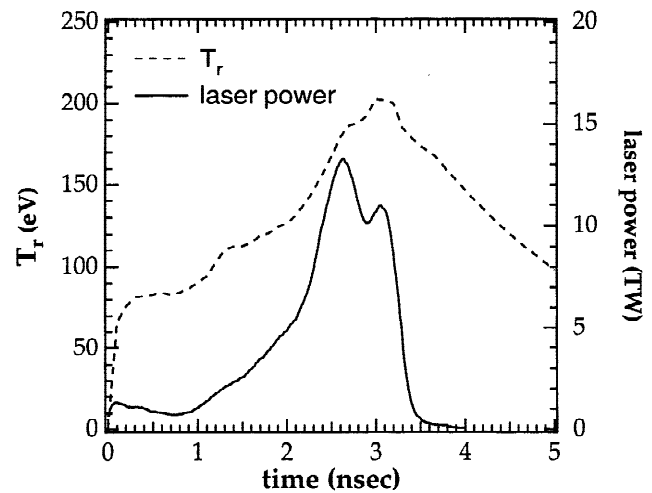

Fig. 2. Normalized perturbation growth factor vs. wavelength at 3.4 ns for the embedded interface (ei) and ablation interface (ai) experiments. The corresponding simulated curves are based on 1-D HYADES hydrodynamic calculations. The $\lambda = 30$-, 70-, and 100-μm ablation-front data were obtained from previous experiments done on Nova (Remington *et al.*, 1992, 1995). The simulated growth factors decrease with increasing wavelength past the limit of 100 μm shown in this plot.
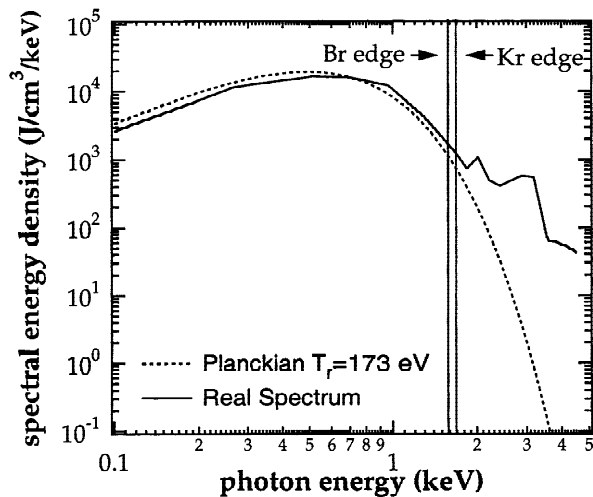
Fig. 4. The hohlraum is not in perfect thermal equilibrium because the laser intensity varies during the drive pulse and the time scale is too short for equilibrium to be reached. Therefore the measured spectrum of the X-ray drive (solid curve) is not purely Planckian (dashed curve).

tudes, a gated x-ray framing camera (Budil *et al.*, 1995) was used to record a series of radiographs of the target. Embedded interface targets were studied with single-mode initial perturbations at wavelengths of $\lambda = 10, 20, 50$, and $100\ \mu m$ and amplitudes ranging from $\eta_o = 0.5$ to $2.0\ \mu m$ while the ablation front targets consisted of side-by-side $\lambda = 20$ and $50\ \mu m$ perturbations with an initial amplitude of $\eta_o = 0.5\ \mu m$. To complete the ablation front data set, results from the prior experiments of Remington *et al.* (1995) are included here.

2.2. Simulations

The purpose of this study was to develop a predictive capability based on modeling with one-dimensional (1D) simulations for the linear regime and early nonlinear regime of a perturbed interface undergoing a series of shocks and accelerations. In the linear regime, where amplitudes, η, are typically less than 10% of the wavelength, λ, the instability growth and hydrodynamics are separable. This allows the instability growth to be calculated from a time-dependent acceleration profile generated from a 1D calculation of the gross hydrodynamics of the system. With this as a starting point we used the 1D radiation-hydrodynamics code, HYADES (Larsen & Lane, 1994), to model the hydrodynamic behavior of the previously described experimental packages. The hydrodynamic calculations generated the time-dependent acceleration, velocity, and position of the targets. The experimental and simulated position trajectories for the embedded interface configuration (triangles and dashed line, respectively) are shown in Figure 5, along with the simulated acceleration profile (solid line). The results of the 1D hydrodynamic calculations, including density, pressure, temperature, and ionization levels are shown in Figure 6. The simulations were post-processed to calculate the perturba-

tion amplitude as a function of time. This quantity was converted to a growth factor (GF), the ratio of the amplitude of the perturbation at a given time to its initial amplitude, for comparison with the data, thereby taking into account the effect of the finite instrument resolution.

A major advantage of working with 1D codes is the ability to rapidly observe the changes caused by varying the parameters of the simulation. Some of the most important of these parameters include the method of zoning, the equation of state (EOS), the ionization and opacity models, and the method of energy deposition. We will briefly discuss and illustrate the sensitivity of the results to these parameters below.

Based on the convergence of the simulations, we chose to use 100 zones for these simulations, 70 in the CH(Br) ablator and 30 in the Ti payload. This resulted in zone sizes that were sufficiently small to track both temperature and radiative diffusion over appropriate scales. For our simulations the CH(Br) slab was divided into sections of equal mass and the Ti was feathered (at a ratio of about 1.15) into the CH(Br)-Ti interface.

The EOS model used in a simulation can make a dramatic difference in the behavior of the modeled material. A calculation done using a realistic, tabular EOS differs significantly from one using an ideal gas model. We used the SESAME tabular EOS (Kerley, 1972), but the degeneracy effects are included in the in-line QEOS (More *et al.*, 1988) model as well. In either case, a realistic EOS model is required to accurately model the shock trajectory and compression through the various target materials.

We used an average-atom ionization model (Pomraning, 1973) for the radiation opacity calculations. Only minor differences were observed between the average-atom model and a Saha ionization model (Rybicki & Lightman, 1979).
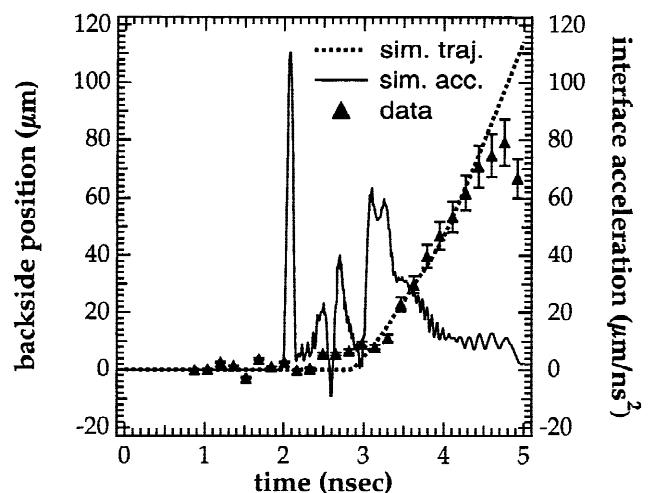

Fig. 5. Experimental trajectory profile of the back side of the Ti foil (triangles) *versus* a HYADES simulation (dotted curve). The calculated acceleration profile is for the CH(Br)-Ti interface from the simulation (solid curve).
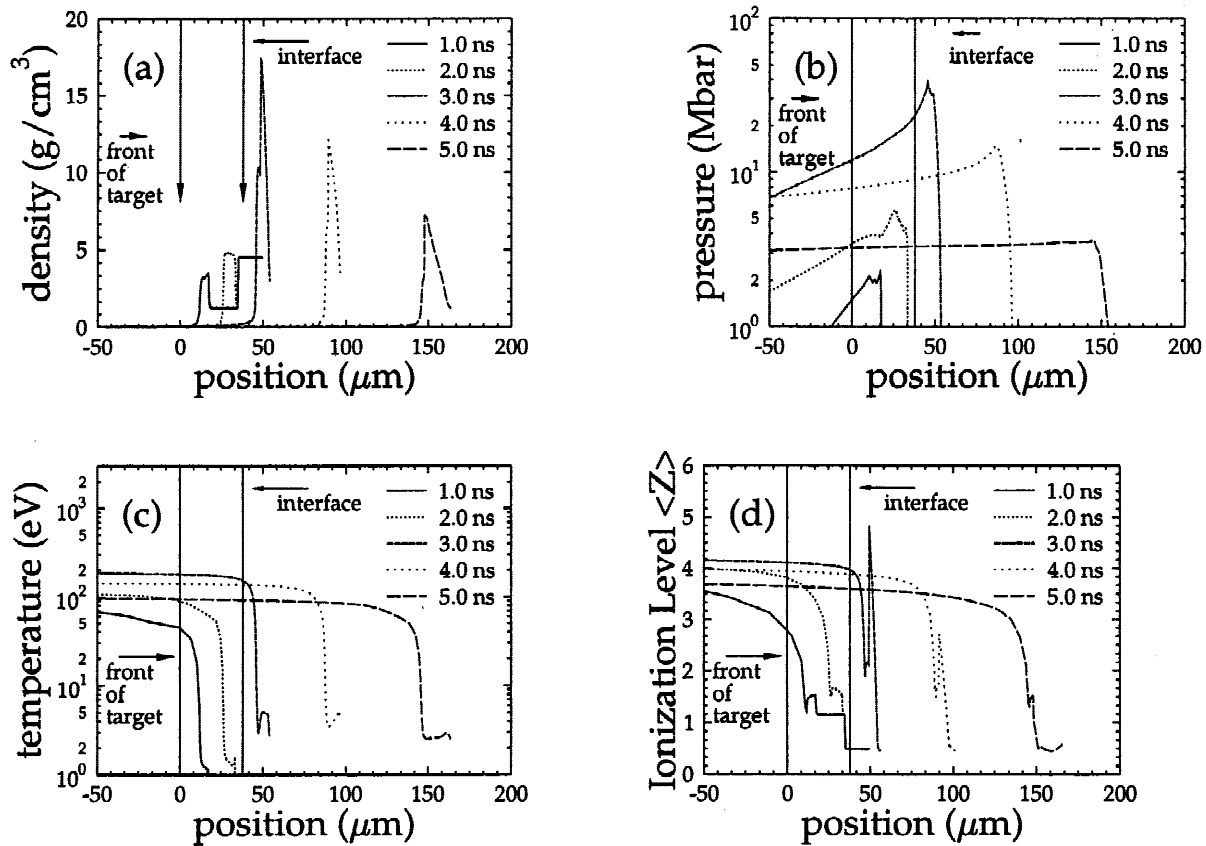
Fig. 6. (a) The simulated evolution of the target density, ρ (g/cm^3), *versus* position (μm) at various times. The front side of the target is initially at 0 μm, the CH(Br)-Ti interface is at 35 μm, and the back side of the target begins at 50 μm consists of CH(Br) from 0–35 μm. (b) The simulated evolution of the target pressure (Mbar) *versus* position (μm). (c) The simulated evolution of the target temperature (eV) *versus* position (μm). (d) The simulated evolution of the target ionization level *versus* position (μm).

2.2.1. Radiation drive spectrum

HYADES uses a multigroup diffusion (Rybicki & Lightman, 1979) method for calculating the effects of radiation transport. It is important to treat the radiation in a multigroup manner because even for a purely Planckian spectrum the mean free path of the photons goes as the cube of the photon energy. We found that 30 photon groups, exponentially scaled from 1 μeV–20 keV, provided good convergence for the simulations. The diffusion of each photon group is calculated separately in HYADES. A radiation temperature drive was used, so the populations of the photon groups were based on a Planckian distribution. This is not a completely accurate treatment of the problem, as the X-rays generated by the gold plasma are not from a source in thermal equilibrium, and there is some excess of higher energy X-rays as shown in Figure 4 (Remington *et al.*, 1995).

The simulations were actually done using Kr ($Z = 36$), which has an L-edge at 1.8 keV (lighter vertical line), instead of Br ($Z = 35$), which has an edge at 1.7 keV, to calculate opacities, but they are very close in absorption. In either case, there is a window below the L-edge where X-rays could penetrate the CH(Br) and preheat the Ti at the interface before the main shock arrives. This preheat-

ing can make the Ti less compressible, thus affecting the target behavior. Figure 7 shows the affect this has on the compressibility of the Ti. For these simulations, we compared a Planckian radiation temperature source with a realistic photon group source and a photon group source that was artificially enhanced at higher energies. This was done to confirm that HYADES could simulate the effects of preheating if it were occurring. As can be seen in Figure 7, with a high enough enhancement of X rays above 1.7 keV, the Ti becomes less compressible. The plots are for a time of 2.2 ns. This change in compressibility can result in a change in perturbation growth because it can modify the target hydrodynamics.

For this work, we performed several simulations with non-Planckian profiles which matched the drive spectra more closely and observed little or no preheating effect. Since the actual drive spectra and T_r profiles were not available for each experiment but the laser powers were, a representative T_r was scaled by the laser power for each experiment using the relationship $P \propto T_r^4$, where P is the laser power. The agreement of the non-Planckian simulations with those using a Planckian source confirmed the validity of the results obtained using a scaled T_r source.
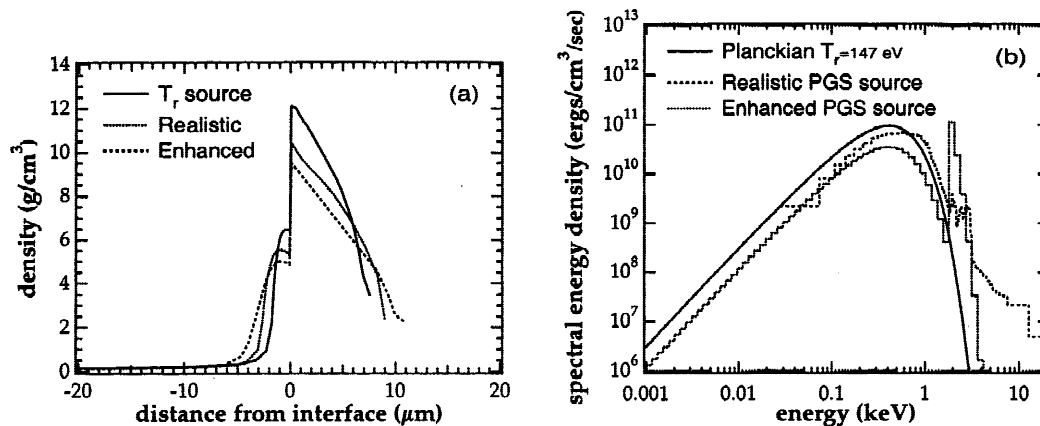
Fig. 7. (a) Calculated density profiles as a function of distance from the CH(Br)-Ti interface for the T_r source (top curve for positive position), a realistic photon group source (PGS) (middle curve for positive position), and a PGS source with an enhanced M-band component (bottom curve for positive position) at a time of 2.2 ns. (b) The spectral composition of the drives used for these simulations at a representative time of 2.2 ns.

3. EMBEDDED INTERFACE RAYLEIGH-TAYLOR MODEL

3.1. Gross hydrodynamics

The goal of this work was to calculate perturbation growth for a variety of initial conditions based on the time-dependent hydrodynamic evolution of the target predicted by simulations using the HYADES code. In Figure 6 we examine the hydrodynamic evolution of the target in detail. The response of the target to the initial shock can be seen in these plots. The density profile shown in Figure 6a shows the propagation of the shock through the material. The CH(Br) is compressed by the passage of the shock and eventually (in ∼2 ns) reaches four times its normal density (see Fig. 6a). Once the shock reaches the interface, the Ti begins to move and also reaches a maximum compression of roughly four times its normal density. When the shock reaches the rear surface of the Ti, the target begins to move and decompress. The pressure profiles shown in Figure 6b show similar behavior but show the ablated CH(Br) as a pressure profile decaying from the front of the target. The pressure reaches a peak of 40 Mbar at the interface and decays slowly behind the shock. This is in contrast to the density, which rapidly decreases as material is ablated away behind the shock. The CH(Br) is directly heated by the T_r source and turns into a plasma, which results in mass loss from the front of the CH(Br). It is this ablation of material that can stabilize growth of perturbations at this surface. The temperature profiles shown in Figure 6c illustrate the heating of the target from an initial temperature of 28 meV to a maximum temperature of 180–190 eV. The high temperature plasma generated by the X-ray drive can be clearly seen streaming away from the front of the target. The temperature remains high longer than the pressure, which trails off due to decompression of the target (as seen in Fig. 6a).

Our first step was to compare the measured side-on radiograph of the trajectory of the rear surface of an embedded interface target with the results of the HYADES simulation. No perturbations were placed at the embedded interface. A 1D simulation should reproduce this 1D experiment. Using the measured X-ray drive temperature from the hohlraum shown in Figure 3 and a SESAME EOS table (Kerley, 1972) for the CH(Br) and Ti, we observed good agreement between the measured rear-edge trajectory and simulation as shown in Figure 5. The calculated acceleration profile of the embedded interface is also shown. Peak accelerations are ∼60 μm/ns^2, i.e. $6 \times 10^{12} g_0$, where g_0 is the acceleration due to gravity at the surface of the Earth.

3.2. Analysis

3.2.1. Embedded interface perturbation growth

Having confirmed the gross hydrodynamics of our simulations we post-processed the results with a theoretical model to calculate perturbation growth. Using an analytic approach, we calculated the linear regime perturbation growth factors for these experiments using time-dependent parameters from the 1D calculations. The linearized equation governing perturbation growth for imcompressible, inviscid fluids is (Chandrasehkar, 1968; Landau & Lifshitz, 1987)

$$\eta''(t) - \gamma^2 \eta(t) = 0, \tag{1}$$

where η is the perturbation spatial amplitude, $\gamma = \sqrt{Akg/(1 + kL)}$ is the growth rate (Sharp, 1984; Munro, 1988; Mikaelian, 1989; Ofer *et al.*, 1992), $A = (\rho_H - \rho_L)/(\rho_H + \rho_L)$ is the linear regime Rayleigh–Taylor Atwood number, where ρ_H and ρ_L are the densities of the heavy and light materials next to the interface, respectively, g is the acceleration of the interface, $k = 2\pi/\lambda$ is the wavenumber of the

initial perturbation, and $L = \rho_{avg}/(\partial\rho/\partial z)$ is the density gradient scale length. We used $A(t)$, $g(t)$, and $L(t)$, that is, the instantaneous values from the simulation, in our calculations.

We first applied the standard steady-state linear regime approximation for perturbation growth due to a slowly varying acceleration, $g/\dot{g} \ll 1/\gamma_{RT}$, (Chandrasehkar, 1968; Landau & Lifshitz, 1987)

$$\eta(t) = \eta_0 \exp\int_0^{t_1} \gamma\,dt. \tag{2}$$

In these experiments the Ti layer was originally only 15 μm thick and was compressed during the experiment down to 8 μm, so we had to account for finite-foil thickness effects. When a bubble is rising through a semi-infinite fluid, there must be a lateral flow of displaced material around the bubble to account for the displacement caused by the growing perturbation. In the case of a finite fluid, this lateral flow is impeded by the lack of a large reservoir of fluid "above" the growing bubbles. We account for this by correcting the growth rate, γ, via

$$\gamma^2 = \left[\frac{Akg}{1 + kL}\right]f, \tag{3}$$

where

$$f = \frac{\rho_L + \rho_H}{\rho_L \coth(kh_L) + \rho_H \coth(kh_H)}, \tag{4}$$

is a scaling factor to account for the finite thickness of the foil (Remington *et al.*, 1992; Landau & Lifshitz, 1987). Here h_L and h_H are the CH(Br) and Ti foil thicknesses, respectively, defined as the distance from the density maximum of each material to its half-density as a function of time. In our simulations, the CH(Br) was compressed at peak drive to $\sim$10 μm, and the Ti was compressed to $\sim$3 μm, as shown in Figure 6. Typical values of A, L, and f are shown as a function of time in Figure 8. Equation (3) combines the density gradient scale length and the Atwood number in an asymptotically consistent manner. In the limit as $L \to 0$ and $f \to 1$, we recover $\gamma^2 = Akg$ as required.

Since the acceleration profile used in these experiments is neither constant nor slowly varying, it may not be valid to approximate the perturbation amplitude as a function of time as in Eq. (2). A simple $e^{\gamma t}$ growth calculation will tend to overestimate the growth by not taking into account the sometimes negative and often quickly changing accelerations of the target. It is more accurate to numerically solve the second-order ordinary differential equation (ODE) [Eq. (1)] for the amplitude as a function of the growth rate γ. The ODE was solved by using a Taylor series and Eq. (1) to obtain:
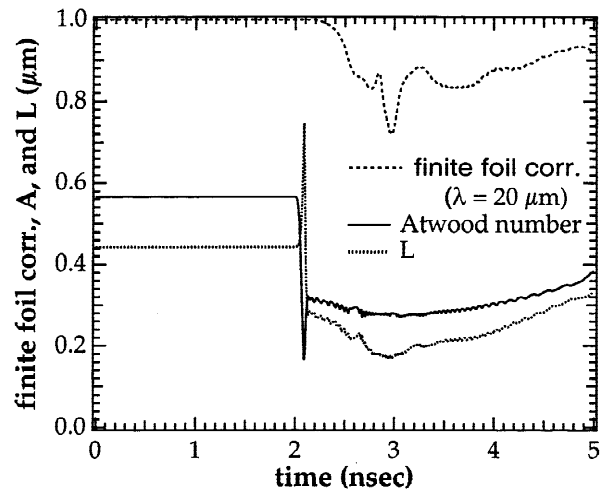

Fig. 8. The perturbation growth calculations used the acceleration profile (see Fig. 5) and the time-dependent Atwood number (solid curve), density gradient scale length, L (dotted curve), and finite foil thickness correction factor, (Eq. (4)) for a $\lambda = 20$ μm perturbation (dashed curve) from the HYADES simulations.

$$\eta(t_n) \approx \eta(t_{n-1}) + \Delta t\,\eta'(t_{n-1}) + \frac{1}{2}\Delta t^2\gamma^2\eta(t_{n-1}), \tag{5}$$

$$\eta'(t_{n-1}) \approx \eta(t_{n-2}) + \frac{1}{2}\Delta t\,\gamma^2\left[\eta(t_{n-1}) + \eta(t_{n-2})\right]. \tag{6}$$

First the accelerations were extracted from the HYADES output file and then $\gamma^2(t)$ and $\eta(t_n)$ were calculated from Eqs. (3), (5), and (6). Δt was the time interval chosen for successive outputs of the hydrodynamic data, in this case 100 picoseconds.

To test the validity of this formula, it was applied to three limiting cases with analytic solutions: (1) an impulsive acceleration represented by $g(t) = \delta(t)v_{final}$ (pure RM), which in the linear regime is known to yield growth linear in time (Richtmyer, 1960; Chandrasehkar, 1968; Meyer & Blewett, 1972; Haan, 1989; Hansom *et al.*, 1990; Brouillette & Sturtevant, 1993; Hect *et al.*, 1994; Peyser *et al.*, 1995), (2) a constant acceleration given by $g(t) = $ constant (pure RT) which in the linear regime yields growth exponential in time (Chandrasehkar, 1968; Sharp, 1984), and (3) a constant negative acceleration, which yields simple oscillatory motion. In all three limiting cases the agreement between the numerical and analytic solutions was excellent. When this prescription was applied to the HYADES hydrodynamic calculations of the Nova laser experiments, good agreement was obtained in the linear regime with the CRT experimental data, as shown in Figure 9. We use the perturbation growth factor, GF $= \eta(t)/\eta_0$, where η is the spatial perturbation amplitude, for comparison with the results of the simulations.

The results shown in Figure 9 demonstrate the validity of using 1D simulations to model perturbation growth. The growth factors calculated based on the HYADES simula-
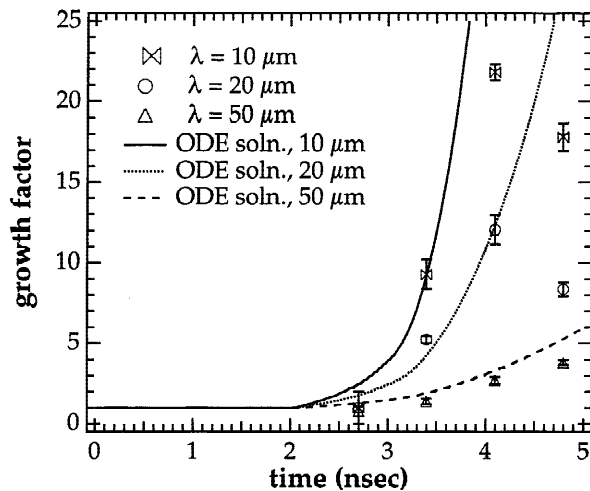
Fig. 9. Observed perturbation growth factor versus time compared with simulation results for embedded interface perturbation wavelengths of $\lambda =$ 10, 20, and 50 μm.

Fig. 10. A comparison of our ODE perturbation growth factor calculation technique and the classical approximation at a wavelength of 20 μm.

tions reproduce the experimental growth reasonably well in the linear regime. The full ODE calculation shows good agreement with experimental data for both $\lambda = 10$ and 20 μm until the experimental data starts to roll over, signaling the onset of nonlinearity. Note that for $\lambda = 10$ μm, an amplitude of 1 μm is already in the nonlinear regime. The calculations agree qualitatively with the data until the roll-off due to growth of second and higher harmonics. For $\lambda = 50$ μm, the calculations slightly over predict the observed growth (with the full ODE calculation being closer than the classical). For $\lambda = 100$ μm, both the experiment and the simulations show very little growth (not shown).

In making this comparison, we implicitly have assumed that the growth factor of perturbation spatial amplitude (from the modeling) is equivalent to the growth factor of optical depth (from the face-on radiography experimental measurements), i.e., $\mathrm{GF}(\mu\mathrm{m}) \approx \mathrm{GF}(\mathrm{OD})$. This equivalence is rigorously correct only for incompressible flows. It is approximately correct here only because the post-shock hydrodynamics are nearly incompressible, and this is when the RT growth is at a maximum, that is, the largest growth occurs in a quasi-incompressible flow.

The full ODE calculation shows closer agreement with the data (i.e. lower growth, see Fig. 10) than the classical steady-state formula due to its better treatment of rapidly changing and occasionally negative accelerations. Notice that the most significant relative deviation between the classical and ODE solutions occurs when the variation in acceleration is greatest (2 to 3 ns). This is because $\mathrm{GF} = e^{\int \gamma \, dt}$ is always growing exponentially with time. But for a shock the perturbation growth is linear in time, and if the acceleration reverses sign, so does $\ddot{\eta}$, so the perturbation growth is reduced. This complete treatment of time dependent accelerations means that the ODE calculation includes growth both
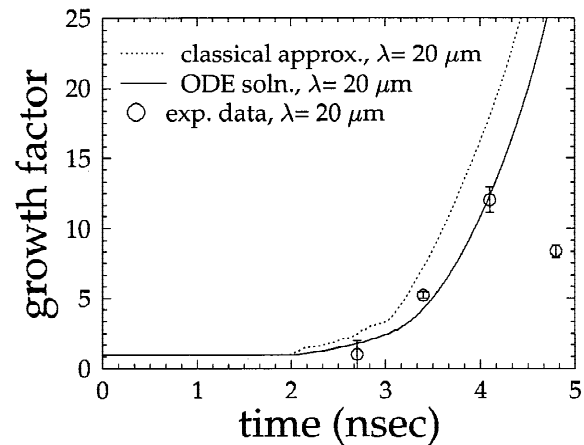
due to the RM and RT instabilities. Even though it neglects RM growth, the classical calculation is not too far off because the shock transit time across the Ti is $\sim$0.8 ns. The RM instability growth begins with the first shock (at 2.0 ns) and then grows linearly in time. The RT instability does not begin until the entire package begins to move as a whole, which does not commence until the shock reaches the rear side of the Ti at 2.9 ns, but its exponential nature leads it to quickly overtake the RM growth.

3.3. The Nonlinear Regime

After confirming our initial results in the linear regime, we turned to different techniques of extending our perturbation growth calculations into the nonlinear regime. We explored the amplitude saturation model of Haan (1989) and a 3rd order perturbation theory expansion (Jacobs & Catton, 1988) (see Fig. 11). The third order perturbation theory expansion is implemented by calculating

$$\eta_1 = \eta_L \left(1 - \frac{1}{4} k^2 \eta_L^2 \right), \tag{7}$$

where η_1 is the amplitude of the fundamental mode, and η_L is obtained assuming linear regime growth [as calculated by Eqs. (5) and (6)]. The third-order results are shown in Figure 11 (lower dotted curve), which qualitatively shows the slowing of the perturbation growth upon entry into the nonlinear regime ($t \geq 3$ ns). But the third-order calculation very rapidly begins to diverge since the perturbation theory has a limited range of applicability. We found that a variation of Haan's theory showed good qualitative agreement with our data. Haan extends a single-mode saturation formula originally devised by Fermi (see Layzer, 1995) to the case of multimode saturation, and generalizes it to non-exponential growth rates using a suggestion of Crowley (1970):
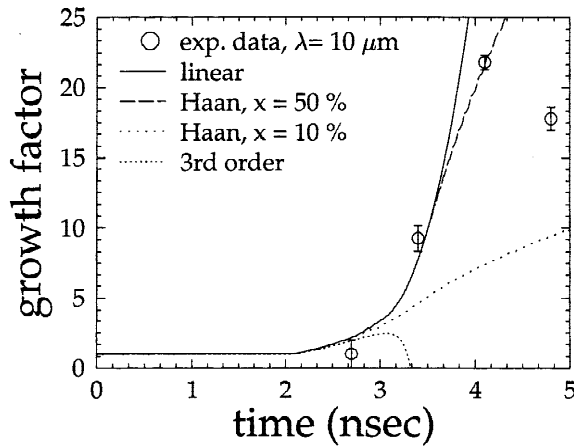
Fig. 11. The linear perturbation growth theory quickly breaks down at later times. By including the effects of saturation, the perturbation growth can be better modeled (Haan, 1989). This figure shows several different approximations in the nonlinear regime. The amplitude saturation criterion of Haan, with a saturation criterion of 50% λ, gives the best agreement with experimental measurement.

$$\eta_{saturated}(t) = x\lambda \left[1 + \ln \frac{\eta_L}{x\lambda} \right], \qquad (8)$$

where x is the percentage of a wavelength at which the amplitude of the perturbation begins to saturate, η_L is the expected linear regime amplitude, and λ is the perturbation wavelength. This is implemented by solving Eqs. (5) and (6) for $\eta < x\lambda$, and Eq. (8) for $\eta \geq x\lambda$. The result is that the RT evolution transitions smoothly to terminal bubble velocity growth at $\eta = x\lambda$. Since our $g(t)$ is not constant, we multiply the asymptotic velocity by the scaling factor $[g(t)/g_{\eta=x\lambda}]^{1/2}$, as analytic theories of the asymptotic nonlinear RT growth give $v_B \propto \sqrt{g\lambda}$ (see Alon *et al.*, 1995).

In our simulations, we found that Eq. (8) with a value of $x = 50\%$ (dashed line) provided the best agreement with our data. This 50% criterion represents an average over the transition from the linear, to the weakly nonlinear, and then finally to the strongly nonlinear regime. Haan's theory is applicable as a limiting saturation case, i.e. in the strongly nonlinear regime, so it is not surprising that the common 10% criterion for the transition from the linear to the nonlinear regime under predicts the observed growth, as can be seen in Figure 11 (middle dotted curve). The value of 50% provides a qualitative sense of the gradual transition from the linear to deeply nonlinear regimes.

4. ABLATION FRONT RT MODEL

In the ablation front experiments, $50 - 60 \ \mu m$ thick CH(Br) foils were ablatively accelerated by the radiation drive shown in Figure 3. Perturbations on the X-ray drive side of the foils were measured as a function of time for evidence of ablative stabilization in the RT growth. For perturbations at a surface exposed to the x-ray drive, such as on the outside of an ICF

capsule, the RT growth is reduced because the outer parts of the perturbations are ablated away ("burned off") by the drive. This leads to a correction to the growth rate, γ, dependent upon the rate of material ablation. In a modified formulation based on the work of Takabe (Weber *et al.*, 1994), the growth rate is approximated by the expression

$$\gamma = \left[\left(\frac{kg}{1 + kL} \right) f \right]^{1/2} - \beta k v_a. \qquad (9)$$

where k, g, L, and f are defined as in Eqs. (3) and (4), $v_a = \dot{m}/\rho$ is the ablation velocity, $\dot{m}$ is the mass ablation rate per unit area, and β is an adjustable, empirically determined parameter which can vary from 1 to 4. Figure 12 shows v_a, L, and g over time as calculated by our simulations. To determine the appropriate β for these experiments, we calculated growth factors for different wavelengths and matched them to the experimental data. To illustrate the affect of β over a range of wavelengths, Figure 13 shows plots of calculated perturbation growth factor *versus* wavelength, that is, dispersion curves, for various values of β. There is a clear dependence of the calculated perturbation growth factor on the value chosen for β, with the growth decreasing as β increases. We found that a value of $\beta = 3$ best fit the full time evolution of the data for our experiments as shown in Figure 14 for $\lambda = 50 \ \mu m$ and $\lambda = 20 \ \mu m$. The estimates of η from Eqs. (2) and (9) apply only for positive values of γ^2 and assume that γ^2 is constant or slowly changing. The profiles of $v_a(t)$ and $L(t)$ vary only slowly in time. The acceleration has one spike at 3 ns due to shock breakout, but subsequently the variation with time is reasonably slow (in contrast to the 4-spike profile of $g(t)$ for the embedded interface target shown in Fig. 5). Hence, for the ablation front calculations, we solve Eq. (2).
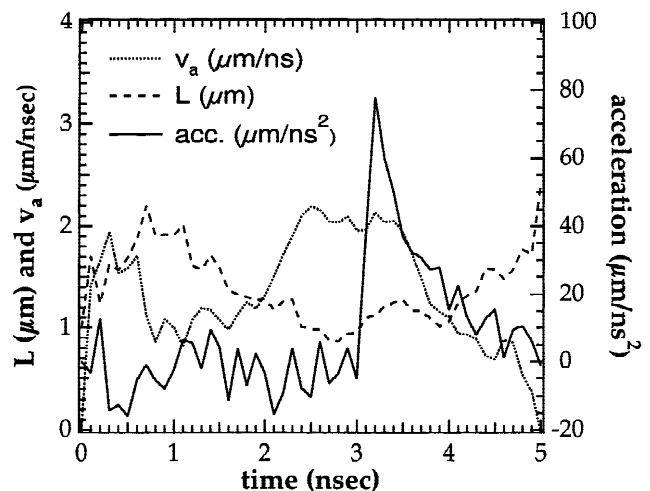

Fig. 12. The ablation front perturbation growth calculations used the time-dependent acceleration (solid curve), density gradient scale length, L (dashed curve), and ablation front velocity, v_a (dotted curve), from the HYADES simulations.
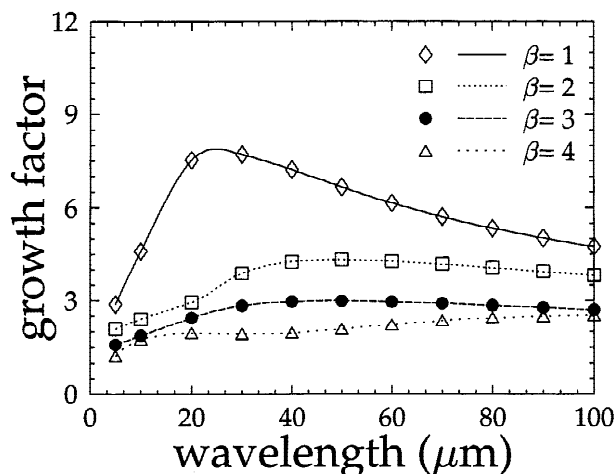
Fig. 13. Simulated ablation front perturbation growth factor *versus* wavelength at 3.4 ns for several values of the Takabe parameter β. The lines are provided as a guide to the eye. Although it is not shown on this plot, the simulated growth factors decrease to zero with decreasing wavelength.

A more rigorous approach to the ablation front problem is given by Betti *et al.*, (Betti *et al.*, 1996; Betti *et al.*, 1998), where the density and pressure profiles at the ablation front from a 1D radiation-hydrodynamics code simulation are fitted to obtain five parameters used in calculating the perturbation growth rate. The normalized density profile ($\xi =$
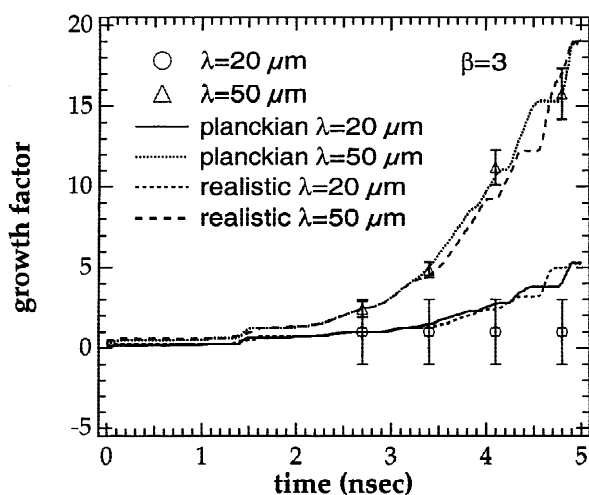

Fig. 14. Calculated normalized ablation front perturbation growth factors (dashed and solid line) and experimental data (circles and triangles). The "realistic" curve is based on a Betti analysis using a realistic drive spectra, and the "planckian" curve is using a Planckian radiation temperature drive. The simulations have been normalized to the data at 2.7 ns. Note the over prediction of growth of both the Planckian and realistic drives at $\lambda = 20\mu$m. This implies that the both the Planckian drive dispersion curve in Figure 15a and the realistic drive Figure 15b do not fall off as rapidly as the data at short wavelengths.

ρ/ρ_a, where ρ_a is the peak density) is fitted using the following differential equation (Betti *et al.*, 1998):

$$\frac{d\xi}{dy} = -\frac{\xi^{\nu+1}(1-\xi)}{L_0}, \tag{10}$$

where y is the spatial coordinate, ν is the thermal conductivity power index ($\kappa \sim T^{\nu}$), and L_0 is the characteristic thickness of the ablation front, which is related to our density gradient scale length $L = \rho/\nabla\rho$ by $L_0 = L[\nu^{\nu}/(\nu+1)^{(\nu+1)}]$. So ν and L_0 are varied until the density profile from the 1D simulation in the vicinity of the ablation front is reproduced by Eq. (10).

The normalized pressure profile ($\Pi = p/p_a$, where p_a is the pressure at the point of peak density) is fit using

$$\frac{1}{\Pi_a^2}\frac{d\Pi}{dy} = \frac{1}{\xi^2}\frac{d\xi}{dy} + \frac{\xi}{\text{Fr}\,L_0}, \tag{11}$$

where $\Pi_a = v_a/(\sqrt{p_a/\rho_a})$ represents the normalized ablation velocity at the point of peak density, and $\text{Fr} = v_a^2/(gL_0)$ is the Froude number, where g is the acceleration at the ablation front (i.e. the "interface" acceleration). So v_a (i.e., Π_a) and Fr (i.e., g) are varied until the pressure profile from the simulation in the vicinity of the ablation front is reproduced by Eq. (11).

With the four parameters ν, L_0, v_a, and Fr the growth rate can be determined using Eq. (8) in Betti *et al.* (1998), which is reproduced in Appendix A for reference.

The exact nature of the ablation front is very sensitive to preheat which is dependent on the drive spectra. We used the result of Remington *et al.* (1995) to determine the spectrum needed to obtain the correct density and pressure profiles. Remington *et al.*, found that to reproduced the inferred level of preheat in the CH(Br) foil required that the X-ray drive spectrum deviate from a purely Planckian black-body by a 10 times enhancement of hard X rays ($h\nu \geq 1.4$ keV) in the first 2 ns.

We used both the analytical fits of Eqs. (10) and (11) as described in Betti *et al.* (1998) and separate numerical fits as described above to obtain values for ν, L_0, v_a, and Fr. We defined the ablation front region to be the material before the peak density, ρ_0, extending from 1.5% to 99% of ρ_0. We found both methods to be in agreement and at a characteristic time of 3.0 ns we obtained values of $\nu = 0.95$, $L_0 = 0.17\ \mu$m, $v_a = 2.3\ \mu$m/ns, and Fr $= 0.7$ for the Planckian drive drive spectrum compared with $\nu = 0.79$, $L_0 = 0.42\ \mu$m, $v_a = 2.9\ \mu$m/ns, and Fr $= 0.67$ for the realistic drive spectrum. These values correspond to interface accelerations of $g = v_a^2/(L_0\text{Fr}) = 40\ \mu$m/ns^2 and $g = 31\ \mu$m/ns^2, respectively. The definition used for the position of the ablation front in Figure 12 is different than the more general ablation front used in the Betti analysis. In Figure 12, we computed the position of the ablation front as the position where the density was at half of its peak value on the front side of the target. In the Betti analysis, the density and pressure profiles

are fit by Eqs. (10) and (11) and the acceleration, g, of the ablation front is computed as $g = v_a^2/(\text{Fr } L_0)$.

The RT dispersion curves predicted by the Betti theory are shown in Figure 15. The differences between using either a Planckian drive or a more realistic source are quite striking. Notice the difference in the location of the peak growth rate between Figures 15a and 15b. The Planckian drive implies a peak at a shorter wavelength than experimentally observed, while the realistic drive of Remington *et al.* yields a dispersion curve with a peak near 50 μm in agreement with the experimental data (see Fig. 2). It should be noted that our simulations do not use sophisticated opacities but rather a simple average ion model and so we do not expect the agreement with Figure 2 to be perfect. To our knowledge, this is the first comparison of the Betti theory to indirect-drive ablation-front RT data, and our results are quite promising.
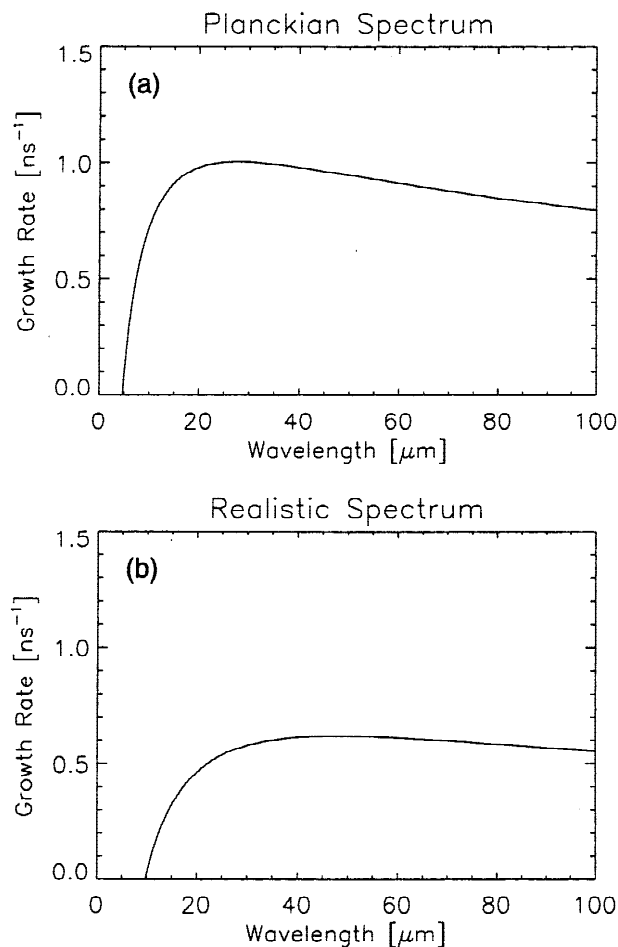

Fig. 15. Dispersion curves of growth rate vs. wavelength generated using the Betti ablation front analysis technique. With a planckian spectrum (a) we find a maximum growth rate at 28 μm (with $\nu = 0.95$, $L_0 = 0.17\mu$m, $v_a = 2.3\mu$m/ns, and Fr = 0.79). Using a more realistic spectrum based on the findings of Remington *et al.* (Remington *et al.*, 1995) we obtain a peak growth rate at 50 μm (with $\nu = 0.79$, $L_0 = 0.42\mu$m, $v_a = 2.9\mu$m/ns, and Fr = 0.67), in agreement with the data and the Takabe analysis with $\beta = 3$ (see Fig. 2).

5. CONCLUSIONS

Comparing the two target types (embedded and ablation front interfaces), allowed us to directly show the influence of ablation. According to theory, embedded interface perturbations should grow faster at shorter wavelengths, which is a potentially serious problem for ICF when considering that even precisely machined ICF targets would have some surface roughness, but ablation should stabilize these short wavelengths. Figure 2, which compares normalized growth factors for the embedded interface to those for the ablation front, clearly shows the effect of ablative stabilization (Budil *et al.*, 1996).

We have found that the 1D Lagrangian, radiation-hydrodynamics code HYADES used together with incompressible hydrodynamic theory can be used to predict the perturbation growth due to the RT instability under a variety of experimental conditions. This approach strengthens both the validity of the simulations and the theoretical models. The 1D model is limited in the behaviors it can describe, but it gives us an excellent opportunity to solidify our theoretical understanding of the inherently complex RT instability.

REFERENCES

ALON, U., HECHT, J., OFER, D. & SHVARTS, D. (1995). *Phys. Rev. Lett.* **74**, 534.

BETTI, R., GONCHAROV, V.N., McCRORY, R.L. & VERDON, C.P. (1998). *Phys. Plasmas* **5**, 1446.

BETTI, R., GONCHAROV, V.N., McCRORY, R.L., SOROTOKIN, P. & VERDON, C.P. (1996). *Phys. Plasmas,* **3**, 2122.

BROUILLETTE, M. & STURTEVANT, B. (1993). *Phys. Fluids A* **5**, 916.

BUDIL, K.S., PERRY, T.S., BELL, P.M., HARES, J.D., MILLER, P.L., PEYSER, T.A., WALLACE, R., LOUIS, H. & SMITH, D.E. (1995). *Rev. Sci. Instrum.* **67**, 485.

BUDIL, K.S., REMINGTON, B.A., PEYSER, T.A., MIKAELIAN, K.O., MILLER, P.L., WOOLSEY, N.C., WOOD-VASEY, W.M. & RUBENCHIK, A.M. (1996). *Phys. Rev. Lett.* **76**, 4536.

CHANDRASEHKAR, S. (1968). *Hydrodynamic and Hydromagnetic Stability*. London: Oxford University Press.

CROWLEY, W.P. (1970). Lawrence Livermore Laboratory report no. UCRL-72650. Technical Report UCRL-72650, Lawrence Livermore National Laboratory. unpublished.

HAAN, S.W. (1989). *Phys. Rev. A* **39**, 5812.

HANSOM, J.C.V., ROSEN, P.A., GOLDACK, T.J., OADES, K., FIELDHOUSE, P., COWPERTHWAITE, N., YOUNGS, D.L., MAWHINNEY, M. & BAXTER, A.J. (1990). *Laser Part. Beams* **8**, 51.

HECHT, J., ALON, U. & SHVARTS, D. (1994). *Phys. Fluids* **6**, 4019.

HERANT, M. & WOOSLEY, S.E. (1994). *Astrophys. J.* **425**, 814.

JACOBS, J.W. & CATTON, I. (1988). *J. Fluid Mech.* **187**, 329.

KERLEY, G.I. (1972). Report LA-4776. Los Alamos, NM: Los Alamos National Laboratory.

LANDAU, L.D. & LIFSHITZ, E.M. (1987). *Fluid Mechanics*, p. 36. New York: Pergamon.

LARSON, J.T. & LANE, S.M. (1994). *J. Quant. Spect. Rad. Trans.* **51**, 179.

LAYZER, D. (1995). *Ap. J.* **122**, 1.

LINDL, J.D. & MEAD, W.C. (1975). *Phys. Rev. Lett.* **34**, 1273.

MESHKOV, E.E. (1969). *Sov. Fluid Dyn.* **4**, 101.

MEYER, K.A. & BLEWETT, P.J. (1972). *Phys. Fluids* **15**, 753.

MIKAELIAN, K.O. (1989). *Phys. Rev. A* **40**, 4801.

MORE, R.M., WARREN, K.H., YOUNG, D.A. & ZIMMERMAN, G.B. (1988). *Phys. Fluids* **31**, 3059.

MULLER, E., FRYXELL, B. & ARNETT, D. (1991). *Astron. Astrophys.* **251**, 505.

MUNRO, D.H. (1988). *Phys. Rev. A* **38**, 1433.

OFER, D., SHVARTS, D., ZINAMON, Z. & ORSZAG, S.A. (1992). *Phys. Fluids B* **4**, 3549.

PEYSER, T.A., MILLER, P.L., STRY, P.E., BUDIL, K.S., BURKE, E.W., WOJTOWICZ, D.A., GRISWOLD, D.L., HAMMEL, B.A. & PHILLION, D.W. (1995). *Phys. Rev. Lett.*, 2332.

POMRANING, G.C. (1973). *The Equations of Radiation Hydrodynamics*. New York: Pergamon Press. pp. 168.

REMINGTON, B.A., HAAN, S.W., GLENDINNING, S.G., KILKENNY, J.D., MUNRO, D.H. & WALLACE, R.J. (1992). *Phys. Fluids B* **4**, 967.

REMINGTON, B.A., WEBER, S.V., MARINAK, M.M. & HAAN, S.W. (1995). *Phys. Plasmas* **2**, 241.

RICHTMYER, R.D. (1960). *Commun. Pure Appl. Math* **XIII**, 297.

RYBICKI, G.B. & LIGHTMAN, A.P. (1979). *Radiative Processes in Astrophysics*. New York: John Wiley and Sons.

SHARP, D.H. (1984). *Physica 12D* **3**.

TAKABE, H., MONTIERTH, L. & MORSE, R.L. (1983). *Phys. Fluids* **26**, 2299.

WEBER, S.V., REMINGTON, B.A., HAAN, S.W. & WILSON, B.G. (1994). *Phys. Plasmas* **1**, 3652.

APPENDIX A. BETTI FORMULA

The following set of equations was published in Betti *et al.* (1998) and is reproduced here for the convenience of those interested.

". . . the asymptotic formula can be written in the following form:

$$\gamma = \sqrt{\hat{A}_T kg + \delta^2 k^4 L_0^2 v_a^2 + \left(\omega^2 - \frac{1}{\xi_l}\right)k^2 v_a^2} - \delta k^2 L_0 v_a - \hat{\beta}k v_a$$

where

$$\hat{A}_T = \frac{\xi_h - \xi_l}{\xi_h + \xi_l}$$

$$\xi_h = (1 + K_1 e^{-K_3/\epsilon})^{-1}$$

$$\xi_l = \mu_0 \left(\frac{1}{\epsilon} + K_2\right)^{-1/\nu}$$

$$\epsilon = kL_0$$

$$\hat{\beta} = \omega \frac{1 + T_1 \epsilon}{1 + T_2 \epsilon}$$

$$T_1 = \frac{\beta_0 - \beta_1}{\beta_2 \beta_0}$$

$$T_2 = \frac{\beta_0 - \beta_1}{\beta_2 \beta_1}$$

$$\omega = \beta_0 \frac{1 + (1 + \hat{A}_T)/(\beta_0 \sinh Fr)}{1 + \sinh Fr}$$

$$\beta_0 = \frac{\Gamma(1 + 2/(\nu + 0.1/\nu^4))}{\Gamma^2(1 + 1/(\nu + 0.1/\nu^4))}$$

$$\beta_1 = \frac{1}{\xi_0 \sqrt{5}}$$

$$\beta_2 = B + \frac{\beta_0^2 + \beta_1^2}{2\delta\beta_1} - \frac{1 + K_1}{2\delta\beta_1}$$

$$\delta = \frac{1}{2Y}\left[K_1 A + \frac{1}{\nu K_2} + \sqrt{\left(\frac{1}{\nu K_2} + K_1 A\right)^2 - 4K_1 \beta_1 Y - \frac{1 + K_1 \nu}{\nu^2 K_2^2}}\right]$$

$$Y = \frac{25}{8} \frac{\xi_0^{2\nu+1}}{2\nu + 3}$$

$$K_2 = [(1 + K_1)\mu_0]^\nu$$

$$K_1 = \frac{1}{\xi_0} - 1$$

$$K_3 = \frac{1 + K_1}{K_1}\left(2\delta Y - \frac{1}{\nu K_2}\right)$$

$$\mu_0 = \frac{(2/\nu)^{(1/\nu)}}{\Gamma\left(1 + \frac{1}{\nu}\right)} + \frac{0.12}{\nu^2}$$

$$\xi_0 = \frac{2\nu + 2}{2\nu + 3}$$

$$A = \frac{\sqrt{5}}{4} \frac{\xi_0^{\nu-1}}{(2\nu + 3)^2}$$
$$\times \left[\sqrt{\frac{2}{5}}\xi_0(12\nu^2 + 25\nu + 18) + \frac{\nu + 2}{2\nu + 3}(8\nu^2 + 20\nu + 17)\right]$$

$$B = \frac{\sqrt{5}}{4} \frac{\xi_0^{\nu-1}}{(2\nu + 3)^2}$$
$$\times \left[\sqrt{\frac{2}{5}}\xi_0(8\nu^2 + 25\nu + 12) - \frac{8\nu^3 + 16\nu^2 + 7\nu + 4}{2\nu + 3}\right].\text{"}$$